A Numerical Study of the Effect of a Mountain Range on a Landfalling Tropical Cyclone

MORRIS A. BENDER, ROBERT E. TULEYA AND YOSHIO KURIHARA

Geophysical Fluid Dynamics Laboratory/NOAA, Princeton University, Princeton, NJ 08542

(Manuscript received 6 September 1984, in final form 18 December 1984)

ABSTRACT

A triply-nested, movable mesh model was used to study the effects of a mountain range on a landfalling tropical cyclone embedded in an easterly flow of ~ 10 m s^{-1}. The integration domain consisted of a 37° wide and 45° long channel, with an innermost mesh resolution of 1/6°. An idealized mountain range with maximum height of ~958 meters was placed parallel to the shoreline. The mountain range, which spanned 19° in the north–south direction and 5° in the east–west direction, was centered in the middle of the channel. Results obtained were compared with a previous landfall simulation, performed without the effect of the mountain range included. In particular, comparison was made of the total storm rainfall, maximum wind distribution and storm decay rate. It was found that the storm filled much more rapidly in the simulation run with the mountain included. The mountain range affected the decay rate through reduction in the supply of latent and kinetic energy into the storm circulation during, as well as after, passage of the storm over the mountain. It was found that a low-level, warm and dry region was produced where the storm winds descended the mountain slope.

In order to better isolate the effect of the mountain on the basic easterly flow, a supplemental integration was performed for the flow without the storm. It revealed that the mountain range caused a significant change in the basic flow over the mountain as well as up to several hundred kilometers downstream and extending considerably above the mountain top. A low-level southerly jet was observed to the west of the mountain base.

1. Introduction

The earth's topography, from a small hill to a large-scale mountain range, influences all scales of atmospheric motion. For the case of the landfalling tropical cyclone, the topography of the particular terrain being transversed has an important impact on most aspects of the storm's behavior such as the storm's movement, decay rate and rainfall distribution. Observationally, studies by Hamuro *et al.* (1969) and Brunt (1968) have shown a strong relationship between the total rainfall associated with landfalling tropical cyclones and the local distribution of orography. Hamuro *et al.* (1969) in their case study showed that maximum hourly rainfall during the landfall of Typhoon Vera in 1959 over Japan was generally located in mountain upslope regions, with the total rainfall amounts strongly related to station elevation. The large amount of precipitation falling in a mountainous region has sometimes resulted in disastrous consequences. For example, torrential rains in excess of 50 cm were directly responsible for thousands of deaths as Hurricane Fifi in 1974 skirted the Honduras coast and interacted with the region's mountainous terrain (Hope, 1975).

Usually the tropical cyclone rapidly weakens as it interacts with the surface orography. As Hurricane David transversed the mountains of Hispaniola in 1979, it abruptly decayed to tropical storm strength before reintensifying on the other side of the island (Hebert, 1980). Brand and Blelloch (1973, 1974) observed significant orographic influences on intensity, speed and direction of movement for typhoons passing over the high mountain ranges of Taiwan and the Philippines. Some of these observed orographic influences were successfully reproduced numerically by Chang (1982) in a primitive equation model which simulated the passage of a tropical cyclone over an island mountain range similar to that of Taiwan.

So far, idealized numerical simulations of hurricane landfall have also been performed by Tuleya and Kurihara (1978), Moss and Jones (1978), and Tuleya, Bender, and Kurihara (1984; hereafter referred to as TBK). Although these experiments were run without orographic effects, they revealed realistic results. For example, in the study of TBK, general characteristics similar to those observed with landfalling tropical cyclones, such as an abrupt change in the low-level winds at the coastline, were obtained. They also showed that the primary cause for storm decay after landfall is the suppression of latent energy. The present study is a continuation of this earlier work. In particular, a landfall simulation similar to the landfall experiment of TBK will be performed with an idealized mountain range placed adjacent to the shoreline. Results obtained will be compared with the previous landfall simulation to determine the effect of this mountain on the decaying tropical

cyclone. Since the enhancement of precipitation and the increased storm decay are important observed orographic influences, as mentioned before, a detailed analysis of these parameters will be made. It is hoped that an improved understanding of these important mountain effects can be obtained by studying this rather idealized and simplified case.

A description of the model, grid system and mountain range will be presented in Section 2. In Section 3 comparison of the two landfall simulations performed with and without the mountain effects will be presented to help explain some additional decay mechanisms associated with the mountain. In Section 4 mountain effects on the basic flow itself will be discussed. Finally, a summary of results and concluding remarks will be presented in Section 5.

2. Experimental design

a. Model used

The triply-nested, movable grid system originally described by Kurihara and Bender (1980) was used for this study. Specific model details are outlined in TBK, and only a brief description is given now. The model is an eleven-level primitive equation model formulated in latitude, longitude and sigma (σ) coordinates. The outermost integration domain spans 37° latitude (5.5–42.5°N) and 45° longitude. A summary of the grid system for each mesh is presented in Table 1. The model physics include a Monin-Obukhov formulation for the surface flux calculation, the Mellor and Yamada (1974) scheme for the vertical diffusion, and cumulus parameterization described by Kurihara (1973). The ocean surface temperature was set equal to 302 K. Land surface temperatures (LST) were determined by the following equation:

$$\mathrm{LST} = 298 - \gamma_s z_*, \qquad (2.1)$$

where γ_s was set equal to 6.7 K km^{-1} and z_* was the surface height. Over both the land and ocean, the surface mixing ratio was equal to the saturated mixing ratio at the surface temperature. Over land this corresponds to a cool, wet surface. As mentioned in TBK, a cool land surface was specified to simulate conditions under the storm's cloud canopy. Miller (1964) has shown that surface temperatures in Hurricane Donna were 2–4 K lower over flat land than over ocean. The value of γ_s was the approximate standard atmospheric lapse rate in the lowest km, averaged for the summer months in the tropics. The value also agreed well with the lapse rate calculated from the model (~6.4 K km^{-1}) in the lower atmosphere over the ocean. Finally, the roughness parameter z_0 was set to 25 cm at all land points.

TABLE 1. Grid system of the triply-nested mesh model used in the landfall experiments.

Mesh	Grid resolution (deg)	Time-step (s)	Domain size: Longitude (points)	Domain size: Latitude (points)
1	1°	150	45° (45)	37° (37)
2	1/3°	50	11° (33)	11° (33)
3	1/6°	25	3 2/3° (22)	3 2/3° (22)

b. The idealized mountain range

The topography used in the present model consisted of an idealized mountain range, beginning at and running parallel to the coastline. It was symmetric in the east–west direction, with a width of 5° longitude and maximum height of about 958 m centered 2.5° longitude west of the coast. The north–south extent of the mountain range stretched 19° latitude and was centered in the middle of the channel. Although this distribution is not representative of the topography of any specific tropical location, mountain ranges paralleling the coast are found on many islands such as Madagascar, the Philippines and parts of Japan. As was mentioned before, it was hoped that the simplified experimental framework used would enable some of the important mountain effects to be isolated and easily analyzed.

The distribution of z_* in the present experiment was first defined for the entire integration domain at the resolution of the finest mesh (every 1/6 degree of latitude and longitude). The values for the coarse resolution were then determined by averaging the heights of fine resolution points that were covered by the area of each coarse-mesh grid box. Therefore, the mountain shape resolved by each mesh was not the same, as shown in Fig. 1. The maximum mountain height for the finest mesh was approximately 958 m, as was mentioned previously, with a corresponding LST of 291.6 K. The mountain top defined by the coarsest mesh was reduced by 83 meters compared to its value resolved by the inner two meshes.

c. Insertion of the orography and land conditions

The previous scheme of TBK was again used to spin up an initially weak vortex over the ocean to a storm of hurricane strength. The vortex was initially centered at 22°N and embedded in an easterly zonal flow of constant angular velocity with a wind magnitude of about 10 m s^{-1} at 20°N. At 52 h the land surface conditions were implemented into the western portion of the computational domain, in a manner similar to TBK. At this time the mountain range was also inserted. The vortex was positioned sufficiently away from the shore at this time so that the wind flow above the mountain range could adjust to the influence of the mountain before the storm's strong

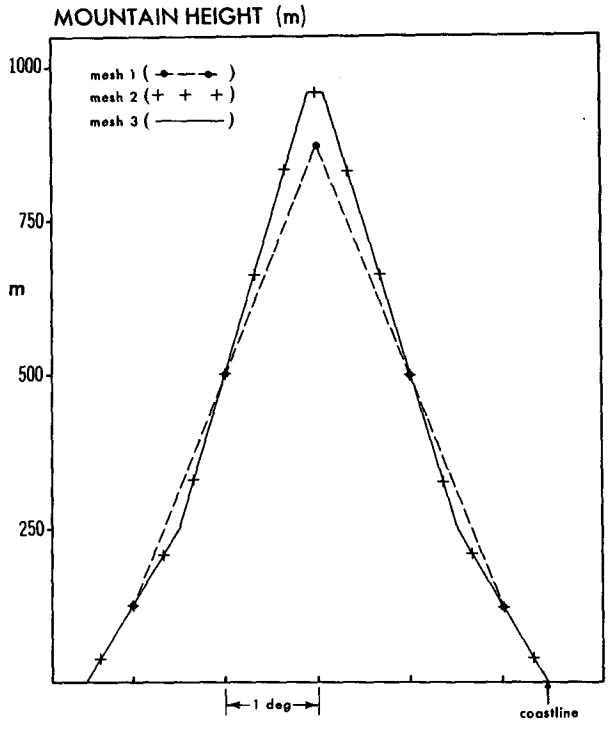

FIG. 1. East–west cross section through the center of the mountain range, showing the mountain height resolved for each of the three mesh resolutions. The large dots connected by the dashed line indicate the height resolved by the coarsest mesh at each grid point. The crosses, which are not connected, indicate the heights for the medium mesh. The solid line shows the mountain shape resolved by the finest mesh resolution.

winds reached the coastline. Insertion of the land conditions into the model was four hours earlier than for the simulation presented in TBK. Thus the present experiment was not strictly a perfect counterpart to TBK. However, we expected these differences would presumably be insignificant, especially after landfall. This was confirmed by a subsequent integration. At the time of land insertion the storm was located about nine degrees longitude east of the shoreline, and the mountain area was confined to the Mesh 1 domain as shown in Fig. 2.

In order to reduce noise that will inevitably occur from insertion of the mountain into the model and the resulting height change of the sigma surfaces, the mass and moisture fields at the new sigma surfaces were obtained before the integration was resumed by linearly interpolating between values at the old sigma levels. This resulted in generation of only a small amount of noise compared with the noise generated by other schemes examined.

During the course of integration, values of z_* and LST at each grid point were kept in a data table for all three mesh resolutions. As the inner grids followed the storm and moved over the mountain during the integration, values of z_* and LST which were covered by the coarse resolution were replaced by their corresponding fine mesh values obtained from the table. A similar procedure was followed as the resolution changed from fine back to coarse.

d. Identification of experiments

For the remainder of the paper, three numerical experiments will be described and analyzed in detail. The landfall experiment performed with the mountain range included will be referred to as Exp. M. Comparison will frequently be made to the previous landfall simulation of TBK (Exp. L298 in their paper) performed without the mountain included. In the present paper this simulation will be identified as Exp. C. A supplemental integration (hereafter referred to as Exp. ZF) was also performed with the same mountain distribution as Exp. M and identical easterly flow initially, but excluding the vortex. For this integration, the movement of the grids was reproduced to correspond exactly with the grid movements made during Exp. M. This enabled proper comparison to be made between Exp. M and Exp. ZF and also allowed an analysis to be made of the flow in the vicinity of the mountain on the finest scale. These three experiments can be summarized as follows,

Exp. M: landfall experiment with mountain range,
Exp. ZF: experiment with mountain and basic flow only,
Exp. C: landfall experiment without mountain effect (Exp. L298 in TBK).

Finally, in the analysis of Exp. M, the sea level pressure over the mountain area was reduced hydrostatically from the surface pressure (e.g., Manabe and

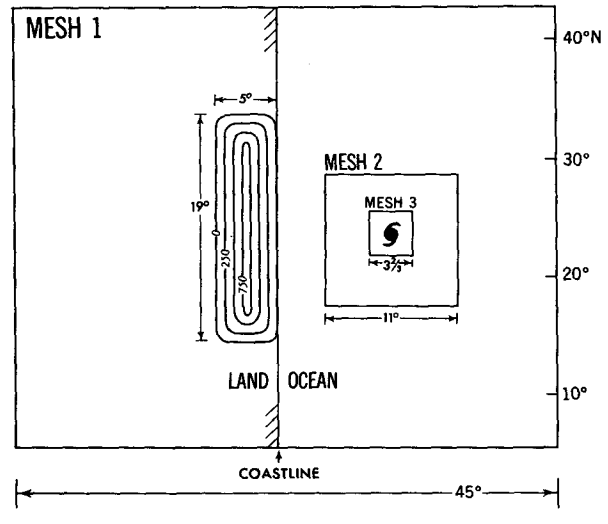

FIG. 2. Experimental domain including the horizontal distribution of the mountain height z_* (m). The positions of the inner meshes and storm center are shown at 52 h, when the topography was first inserted into the integration.

Holloway, 1975), which yielded a smooth sea level pressure field.

3. Numerical simulation of landfall

Before proceeding with an analysis of the landfalling tropical cyclone, we will first describe the flow that existed above the mountain in the absence of the storm. From Fig. 3 we can see the effects the mountain range has on the basic flow at the 1.4 and 6.8 km levels. A rather strong vertical shear in the wind exists between these two heights. For example, on the east side of the mountain range, a strong northerly wind component exists at the upper level. Although a small northerly component can be found over the west side as well, the flow eventually changes direction far downstream from the mountain, as would be expected for mountain flow in a stratified atmosphere (e.g., Smith, 1979). At 1.4 km the flow is basically zonal on the east side of the mountain. However, below this height the wind again exhibits a northerly component. From Fig. 3 we see that the wind, which is maximum above the mountain top, makes a sharp turn to the right on the lee side of the mountain. We will show later in Fig. 15 that this resulting southerly flow extends well downstream from the mountain. Upstream, the effect of the mountain on the flow field appears to be relatively small. According to the study on mountain flow by Pierrehumbert (1984), we would not expect strong blocking of the flow to occur for the mountain height and zonal flow prescribed in Exp. ZF.

a. Comparison with the nonmountain simulation

After implementation of the topography and land conditions at 52 h, Exp. M was continued with the

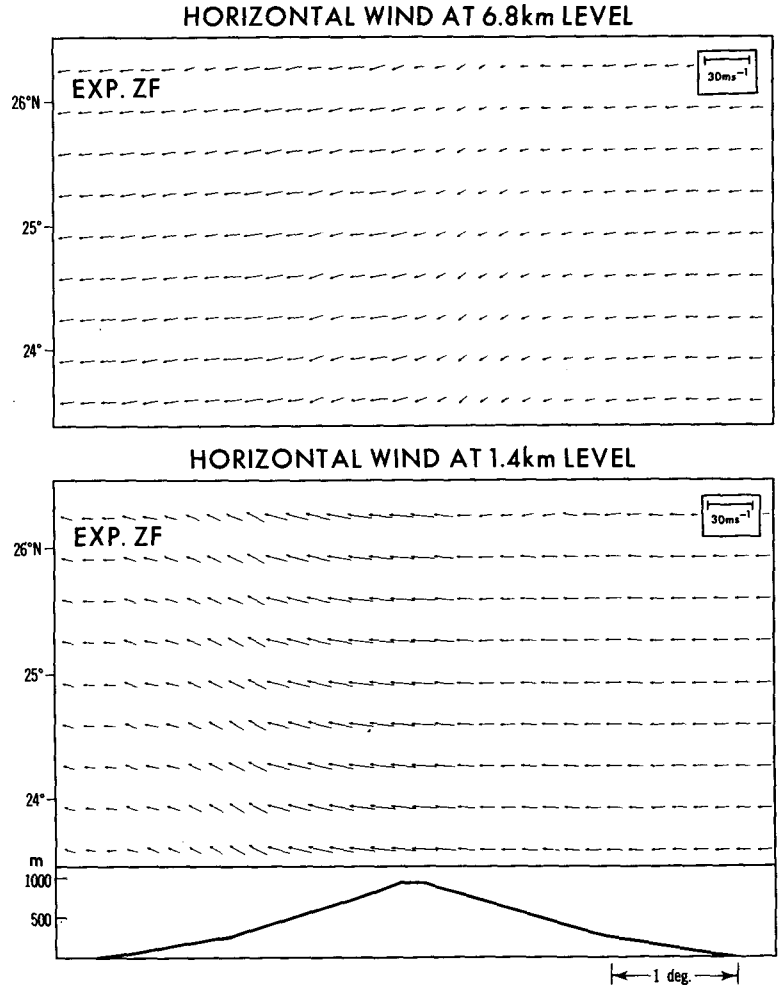

FIG. 3. Horizontal distribution of the wind vectors for the zonal flow experiment (Exp. ZF) at the 6.8 km height (upper) and the 1.4 km height (lower) for the region above the mountain. Vectors are plotted for every other grid row in the latitudinal direction.

same lateral boundary conditions used in Exp. C. Landfall of the hurricane occurred at 78.2 h, with minimum surface pressure and maximum low-level (σ = 0.992) wind at landfall of 960.5 mb and 51 m s^{-1}, respectively. The storm reached maximum intensity about one hour prior to landfall, similar to Exp. C. The time series of minimum sea level pressure and maximum low-level winds is presented in Fig. 4 for both experiments. After landfall, the storm began to weaken rapidly, with the minimum sea level pressure filling about 32 mb in the next 12 h. This compared with a 20 mb fill rate in Exp. C. The rapid fill rate compares with a 12-hour fill rate of ~50 mb for Hurricane David in 1979 as it crossed the high mountains of Hispaniola. During the same period maximum low-level winds dropped from 53 m s^{-1} just prior to landfall to 24.0 m s^{-1} 12 h later. While the central surface pressure tended to eventually level off at about 989 mb by 15 hours after landfall in Exp. C, the weakening continued at a reduced rate for Exp. M. By 20 h after landfall minimum pressure exceeded 1000 mb and maximum surface winds fell below 15 m s^{-1}. Statistical studies by Brand and Blelloch (1973) have shown that the maximum surface winds typically decreased just prior to landfall for typhoons approaching the Philippines. For Taiwan this decrease usually began about 12 h before the typhoons reached the island (Brand and Blelloch, 1974). However, in both cases, reduction of the maximum surface wind continued during the entire time the storms were crossing the islands' mountainous terrain. In the numerical simulation by Chang (1982) of the passage of a tropical cyclone over an island mountain range, the reduction of the maximum surface winds occurred entirely before landfall, with the winds increasing again just prior to and during passage of the storm over the island.

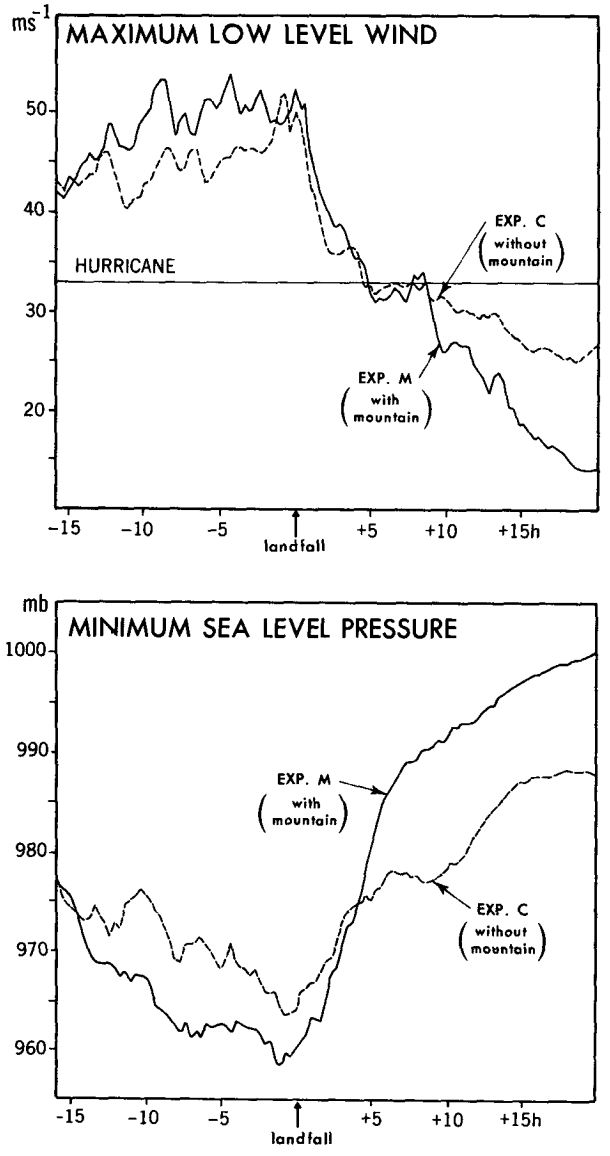

FIG. 4. Time series of minimum sea level pressure (mb) and maximum low-level (σ = 0.992) wind (m s^{-1}) for the two landfall experiments, C and M.

The spatial distribution of maximum low-level winds and the storm tracks for Exp. M and Exp. C are presented in Fig. 5. The inland extent of the hurricane force winds (>33 m s^{-1}) penetrated about the same distance from the coast, (i.e., about 165 km) for both experiments. The maximum low-level winds north of the storm track in Exp. M were slightly stronger up to 150 km inland. However, as the storm continued to move inland across the mountain, the maximum winds in Exp. M eventually dropped below 25 m s^{-1} beyond 375 km from the coast, while the 25 m s^{-1} contour extended to the western side of the figure in the case of Exp. C.

Comparison of the storm tracks (defined by the storm's center of mass) indicate that during the period from landfall to 6.5 h later, when the storm in Exp. M reached the mountain top, it moved about 50 km farther to the south than the storm in Exp. C. On the lee side, the low-level southerly flow produced about a 90 km northward movement of the storm, which is slightly more than double the northward displacement that occurred in Exp. C. Since the east–west translational speed of the storm in both experiments exhibited a natural fluctuation with time (~10% in a period of several hours), comparison of this quantity between the two experiments was difficult unless a sufficiently long time interval was used. In Chang's (1982) study the storm's translational speed increased significantly prior to landfall, with the storm center moving cyclonically around the northern end of the island. However, in his study the storm movement was largely influenced by the storm's latent heating and the limited latitudinal extent of the mountain range, which was comparable to the size of the storm circulation. In addition, a comparison

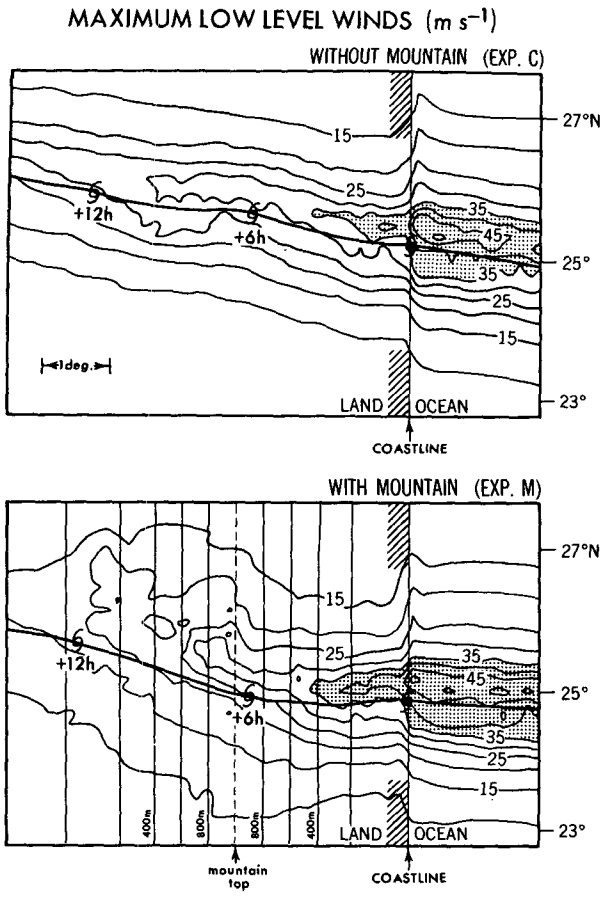

FIG. 5. Horizontal distribution of maximum low-level (σ = 0.992) wind (m s^{-1}) obtained at each grid point during the passage of the tropical cyclone for Exp. C (upper) and Exp. M (lower). The shading indicates wind speeds greater than 35 m s^{-1}. The land area is to the west of the indicated coastline. Height of the mountain range at 200 m intervals as well as location of the mountain ridge is also presented for Exp. M. Storm tracks are shown for the two experiments with the position of the storm center every six hours and number of hours after landfall shown.

between the two numerical results is further complicated by the differences in mountain height, width, magnitude of the basic flow, the land–sea distribution, and the model's horizontal and vertical resolution.

Analysis of the wind fields for Exp. M revealed that after landfall the storm's circulation center became vertically tilted with height. For example, when the storm was just east of the mountain top, the storm's circulation center at the 8.1 km height had become about 20 km displaced to the northeast of the center at the 900 m level. For Exp. C no vertical tilt in the circulation center was seen at any time after landfall. By 8 h after landfall, the upper-level center of circulation was located 35 km directly to the east of the center at 900 m. Two hours later the 8.1 km center had also shifted about 20 km south as well as 45 km east of the low-level center. Finally, a southeastward tilt of about 75 km was observed by the time the storm approached the west edge of the mountain, i.e., 12 h after landfall. Throughout this entire period, the position of the lower-level circulation center remained near to the center of mass or location of minimum pressure. An example of this will be shown in Fig. 12. A decoupling of the circulation centers with height was noted by Chang (1982) in his model study.

It is interesting to note from both Figs. 4 and 5 that a noticeable difference in the storm intensity between the two experiments occurred well before landfall. The observations by Brand and Blelloch (1973, 1974) have also indicated that typhoons making landfall on Taiwan and the Philippines often have undergone noticeable increases in intensity during the period between 48 and 20 h prior to landfall. Although it is not certain whether this is a direct result of the islands' topography, which reaches over 2000 m height at some locations, the effect of mountains on atmospheric flow is certainly observed often well upstream (e.g., Smith, 1979). Also, Suda (1972) indicated that high mountains over Indochina induce mountain waves which possibly influence typhoon formation and movement over a vast area far from the mountain. Although no strong blocking of the flow occurred in our experiment, as mentioned previously, the mountain range did alter the upstream zonal flow slightly with generation of a small northerly component in the flow field as well as a slight reduction (30 cm s^{-1} at some locations) in the zonal flow observed hundreds of kilometers upstream. The storm center in Exp. M began to deviate to the southeast relative to the position of the storm center in Exp. C about 16 h before landfall. At landfall the storm center in Exp. M was about 35 km to the south of the landfall position in Exp. C. Also, the boundary layer moisture field was slightly more moist in Exp. M from the coastline up to about 400 km upstream, with an average increase in the mixing ratio of about 0.1 gm kg^{-1}. This increase may have resulted from a convergence of moisture east of the mountain range as the zonal flow was decelerated at the lower levels.

b. Mountain effect on the precipitation

The effect of the mountain range on the precipitation is discussed in this subsection. We can see from Fig. 6 that both experiments exhibit an enhancement of heavy precipitation (i.e., >10 cm, shaded area) to the right of the storm track immediately after landfall, probably related to the increased coastal convergence. In Exp. M, the orographically-forced ascent of the winds north of the track resulted in an extension of the 10 cm contour for most of the

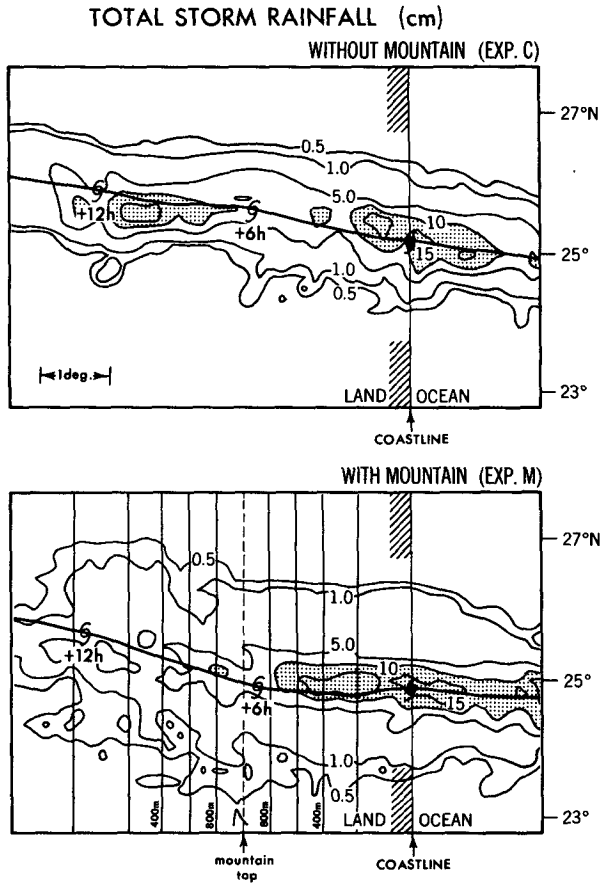

FIG. 6. Distribution of the storm total rainfall (cm). Total rainfall greater than 10 cm is shaded. See Fig. 5 for further information.

distance up the mountain. Note the immediate dropoff of the 5 cm contour north of the track at the mountain ridge with a broadening of the 5 and 1 cm contours south of the track just west of the mountain top. As mentioned in Section 1, high correlations have been frequently observed with rain maxima associated with landfalling tropical cyclones and the orography of the region (e.g., Brunt, 1968; Hamuro *et al.*, 1969). However, when comparison of Fig. 6 is made with their observed rainfall maps, we find that the more complex topography greatly complicates the rainfall distribution. Another interesting feature in Fig. 6 is the increase both before and after landfall in the area covered by the 0.5 and 1.0 cm contours, respectively, in comparison to Exp. C. We can also notice an increase in the total amount of precipitation before landfall in Exp. M, apparently associated with the increased storm intensity.

The precipitation rates, calculated during one model time step, were also analyzed and are presented in Fig. 7. Before landfall, the areas of heaviest rain (greater than 7.2 cm h^{-1}) were found in convective regions that tended to rotate cyclonically around the storm center. A similar behavior was also observed in Exp. C during the entire simulation. In the presence of the mountain range the region of heaviest rainfall tended to shift to the north of the storm center just prior to landfall, where its position relative to the storm center remained for the next several hours as the storm climbed the mountain slope. At 82 h the maximum rainfall rate was 8.4 cm h^{-1}, located 37 km directly north of the storm center. The area of light precipitation was considerably broadened as compared with Exp. C (see Fig. 4 of TBK). After 82 h, the entire precipitation region began to shift slowly to the east of the storm center. Also, by 84 h the area of heaviest rainfall rate was greatly reduced. At 87 h we see that the precipitation was most intense southeast of the storm where the low-level wind was upslope, and it was very light to the north and west. Finally, by 92 h the storm became quite disorganized with the regions of significant rainfall intensity much reduced in area.

Most of the enhancement of precipitation north of the storm center at 82 h was directly due to forced lifting of moist air up the mountain. On the other hand, it was observed in the analysis of Exp. C (see Fig. 9 of TBK) that a stable layer over the cool land surface contributed to the reduction of precipitation intensity after landfall. This stabilizing effect due to the cool land surface was retarded with the inclusion of orography. For instance, when the storm center was still 125 km to the east of the position at 82 h, the lapse rate of the saturated equivalent potential temperature in the upslope region, averaged over several grid points and calculated for the lowest km above the surface, decreased from 9.6 K km^{-1} for Exp. C, to 3.8 K km^{-1} for Exp. M. This made the region more favorable for convection when the storm reached the area.

c. Mechanisms to enhance decay

The primary decay mechanism of the tropical cyclone after landfall has been shown by observational studies to be the reduction of surface evaporation over the land. Some of these observational results are summarized by Anthes (1982) and by Simpson and Riehl (1981). Numerical modeling studies (Tuleya and Kurihara, 1978; Anthes and Chang, 1978) have also confirmed the importance of the suppression of evaporation for tropical cyclone decay. From the comparison of Exps. M and C, it is clear that the inclusion of topography can make an additional significant impact on storm decay.

To investigate the possible causes of this enhanced decay in Exp. M, moisture and kinetic energy budgets were analyzed for the period 71–96 h for a 3.5 × 3.5° square domain centered on and moving with the storm. This domain can be considered represen-

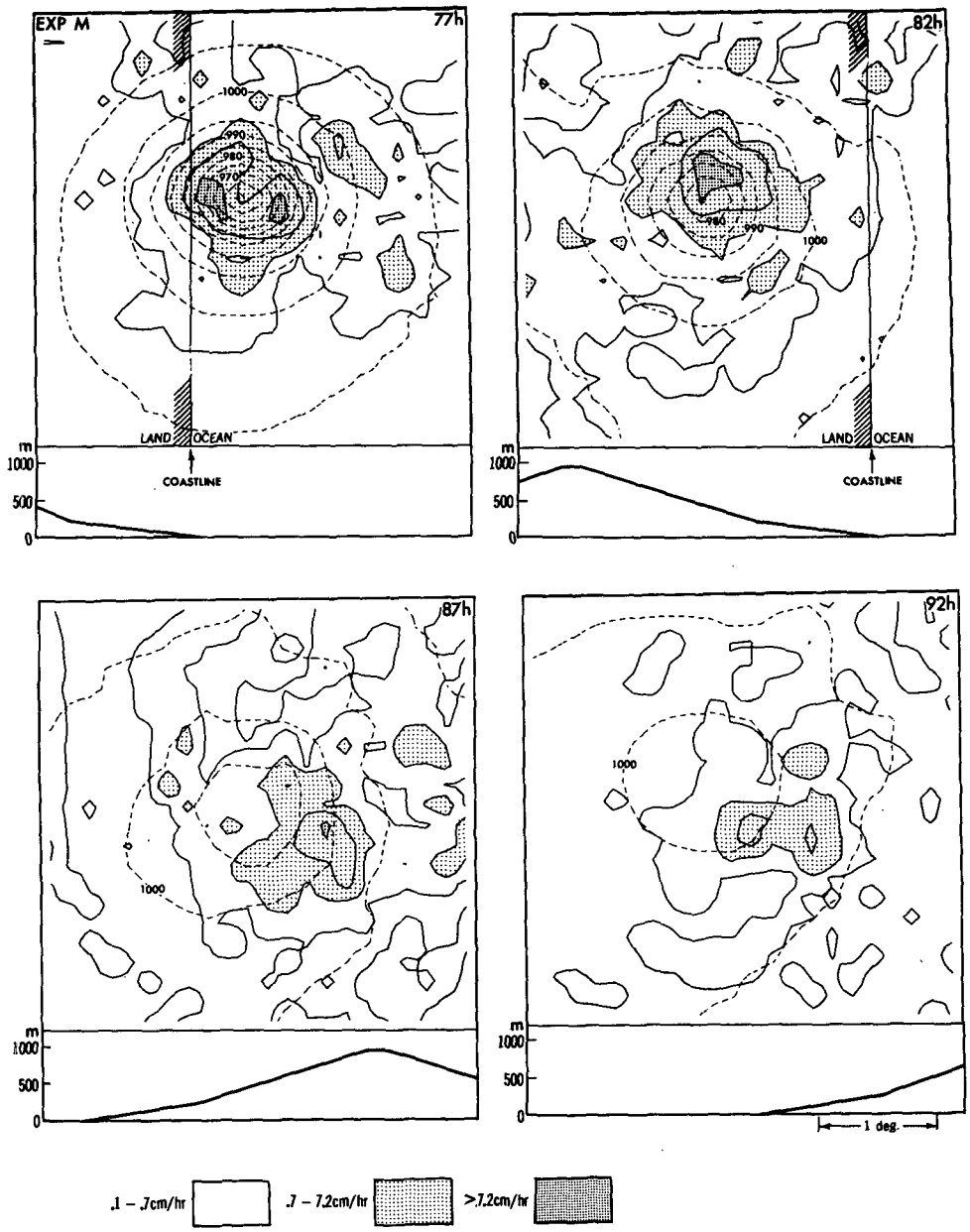

FIG. 7. Rainfall intensity in the finest mesh area for Exp. M at 77, 82, 87 and 92 h. The shading legend indicates intensity in cm h^{-1}, with an additional contour of 2.9 cm h^{-1} drawn within the lighter shading. The dashed lines are the isobars (mb) of the surface pressure reduced to sea level. Land is to the west of the indicated coastline. The height of the mountain range (m) is shown as a function of longitude at the bottom of each figure.

tative of the immediate storm region. The equation for the change of precipitable water can be written as:

$$\overline{\frac{\partial}{\partial t}\int p_* r \frac{d\sigma}{g}} = -\overline{\int \nabla\cdot[(\mathbf{V}-\mathbf{C})p_* r]\frac{d\sigma}{g}} + \overline{\mathrm{EVAP}} - \overline{\mathrm{PREC}} + \overline{\mathrm{HDIF}}. \quad (3.1)$$

The symbols are the same as defined by TBK; i.e., the overbar denotes an area average, **C** the mean storm movement vector, **V** the vector wind, EVAP the evaporation rate, PREC the precipitation rate and HDIF the convergence of water vapor into the storm region through subgrid-scale horizontal diffusion. The term on the left-hand side denotes the change of total precipitable water, and the flux convergence of water

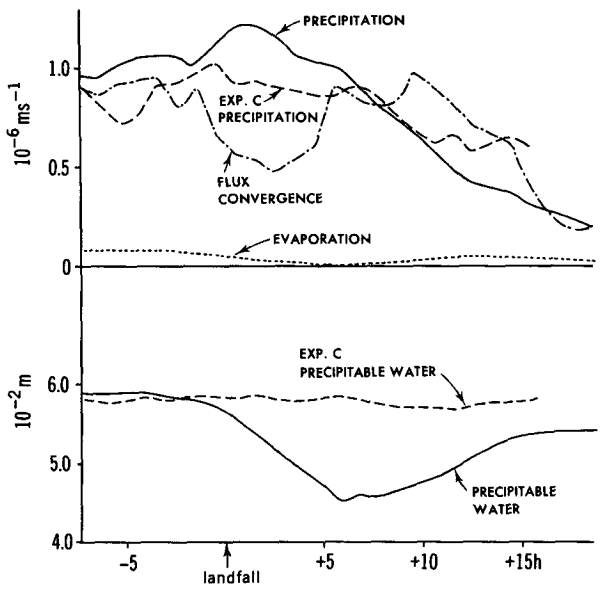

FIG. 8. Moisture budget for Exp. M for the 3.5 × 3.5° domain relative to the moving storm. The precipitation rate, expressed in 10^{-6} m s^{-1}, is plotted as positive for the purpose of comparison and may be converted to cm h^{-1} by multiplying by 0.36. The horizontal diffusion term HDIF was too small to be plotted. All quantities are calculated and plotted every hour, with the abscissa indicating the number of hours before and after landfall. For comparison, the precipitation rate and precipitable water for Exp. C are indicated by the long dashed lines.

vapor into the storm is represented by the first term on the right-hand side. The value of C was considered constant and set to −10.8 m s^{-1} westward and 1.75 m s^{-1} northward. The time variation for all terms except HDIF, which was too small to be plotted, is presented in Fig. 8, with the precipitable water plotted below. For comparison purposes, the precipitation rate and precipitable water for Exp. C were also presented. The precipitation rate sharply increased in comparison to Exp. C from the period just prior to landfall, when the storm's strong winds northwest of the center first reached the mountain slope, to about 6.5 h after landfall. During this period the precipitable water began to decrease sharply, reaching a minimum at about the time the storm transversed the mountain top. As the storm ascended the mountain, the flux convergence term was reduced partly because the air fluxed into the storm region was drier. Another cause for the reduction of the flux convergence of moisture is related to the wind field in the planetary boundary layer. The distribution of the wind field at model level 10 (~200 m above the surface) at 82 h, or four hours after landfall, is shown in Fig. 9. Note that a strong easterly component existed at the upper left-hand side of the figure especially in comparison to Exp. C (see Fig. 2 of TBK). This resulted in strong export of moisture out of the storm area. A similar effect was found at other model levels in the boundary layer. Upon examination of the hourly synoptic wind maps, the above feature in the boundary layer wind first appeared around 80 h (two hours after landfall) when the western boundary of the storm domain was nearing the 800 m mountain contour. Thus, the resulting reduction in the net flux convergence of moisture combined with the sharp increase of precipitation north of the storm center caused a reduction in precipitable water. The precipitable water increased again as the storm descended the western side of the mountain, although it recovered to a value that was considerably less than before landfall.

The aforementioned strong easterly component above the mountain ridge to the northwest of the storm (Fig. 9) appears to be partly due to the influence of the mountain on the basic flow, as observed in Exp. ZF (Fig. 3). In addition, the interaction of the tropical cyclone itself with the mountain could have contributed to this effect. For example, comparison between Exps. M and C of the boundary layer divergence fields indicates that there was a tendency in Exp. M for the divergence (convergence) to increase (decrease) in the region of upslope wind. This suggested vortex compression existed in the boundary layer, with the exception of the areas of enhanced

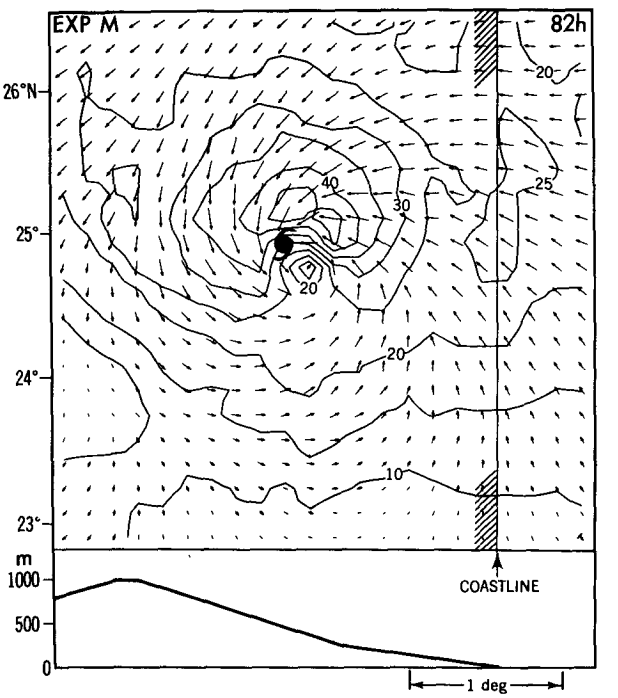

FIG. 9. Distribution of the horizontal wind vectors and wind speed (m s^{-1}) at model level 10 (σ = 0.977) in the finest mesh at 82 h for Exp. M. The mountain height (m) is plotted at the bottom of the figure. The center of the storm, defined by the sea level pressure field, is indicated by a hurricane symbol.

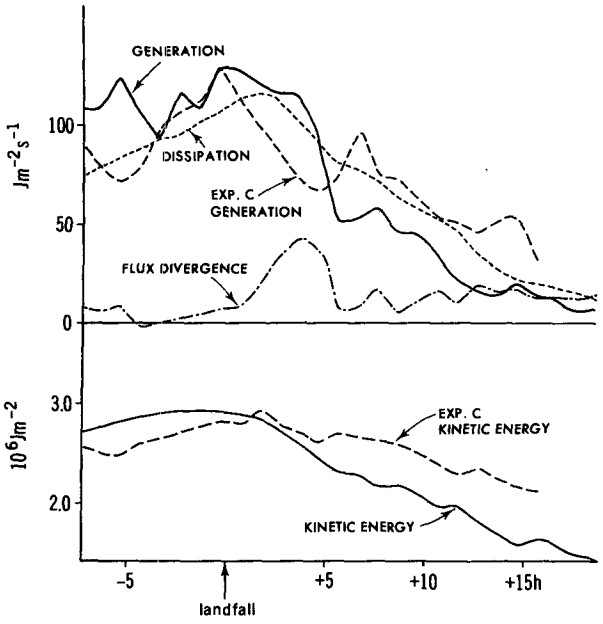

FIG. 10. Kinetic energy budget for Exp. M for the 3.5 × 3.5° domain relative to the moving storm. The dissipation and flux divergence, negative components in the budget, are plotted with their signs reversed. All quantities are calculated and plotted every hour, with the abscissa indicating the number of hours before and after landfall. For comparison, generation and total kinetic energy for Exp. C are indicated by long dashed lines.

precipitation where the convergence increased. It was also found that the increase of the divergence accompanied an increase of anticyclonic vorticity northwest of the storm as it ascended the mountain.

The kinetic energy budget computed for the same storm region is presented in Fig. 10. The kinetic energy equation can be expressed as follows:

$$\overline{\frac{\partial}{\partial t}\int p_*\left(\frac{u^2+v^2}{2}\right)\frac{d\sigma}{g}} = -\overline{\int \nabla\cdot\left[(\mathbf{V}-\mathbf{C})p_*\left(\frac{u^2+v^2}{2}\right)\right]\frac{d\sigma}{g}} - \overline{\int p_*\mathbf{V}\cdot\nabla_p\phi\,\frac{d\sigma}{g}} + \overline{\int p_*\mathbf{V}\cdot\mathbf{F}_v\,\frac{d\sigma}{g}}. \quad (3.2)$$

Once again, the overbar denotes the storm area average, u and v the zonal and meridional wind components, $\nabla_p\phi$ the geopotential gradient on a pressure surface and $\mathbf{F}_v$ the frictional force. The quantity on the left is the time change of the vertical integral of kinetic energy per unit area. The terms on the right side are the relative flux convergence of kinetic energy per unit area, the vertical integral of the generation of kinetic energy per unit area, and the vertically-integrated dissipation of kinetic energy per unit area, respectively. The generation of kinetic energy for Exp. C is also plotted in Fig. 10 with the kinetic energy for both Exps. M and C plotted at the bottom. We clearly can see a sharp increase in the flux divergence term during the period between two and six hours after landfall. Apparently the strong easterly component of the wind above the mountain ridge caused a large export of kinetic energy away from the storm. The dissipation and generation terms both increased for the first several hours after landfall. The net result from all three terms was a sharp decrease of kinetic energy.

As we noted previously from Fig. 4, the storm continued to weaken after crossing the west base of the mountain range well after landfall. The moisture fields at 12 h after landfall, presented in Fig. 11, were analyzed in order to find the reasons for this continued decay. In order to enhance the portion of the atmosphere near the surface, the vertical coordinate in the cross sections in Fig. 11 and all others presented in the remainder of the paper is the square root of height in meters. In this figure, vectors of moisture flux were plotted. In Exp. C, the strong easterly flow served to advect moist low-level air well inland from the shore with values of mixing ratio exceeding 21 g kg^{-1} found in the lower boundary layer north of the storm center. Much of this air was eventually brought into the storm area. Indeed, as shown in the cross section through the storm center, low-level air with mixing ratios of 20 g kg^{-1} or higher is fluxed into the storm's center region in Exp. C. In contrast, the moisture content of the low-level air advected into the storm in Exp. M was significantly reduced by the mountain. Although evaporation from the land surface tended to moisten this air somewhat as it descended down the mountain, it was still considerably drier than in Exp. C. Figure 11 also shows that the moisture flux above the storm center in Exp. M was considerably weaker by 90 h. It was already noted that by this time the storm in Exp. M appeared much more disorganized than in Exp. C. In particular, we can see from Fig. 12 that the upper-level (8.1 km) circulation center was displaced about 75 km to the southeast of the center of circulation in the lower levels. As was mentioned in Section 3a, the storm circulation center in Exp. C remained vertical after landfall. Since the vertical tilt of the wind field in Exp. M became large as the storm approached the western base of the mountain it may have contributed to the continuing decay process.

To summarize, the increased decay of the storm in Exp. M relative to Exp. C was primarily a result of the reduction in the supply of latent and kinetic energy into the storm region. As the storm ascended the mountain, drier air over the mountain was fluxed into the storm. The resulting reduction of the flux convergence of moisture was enhanced by another

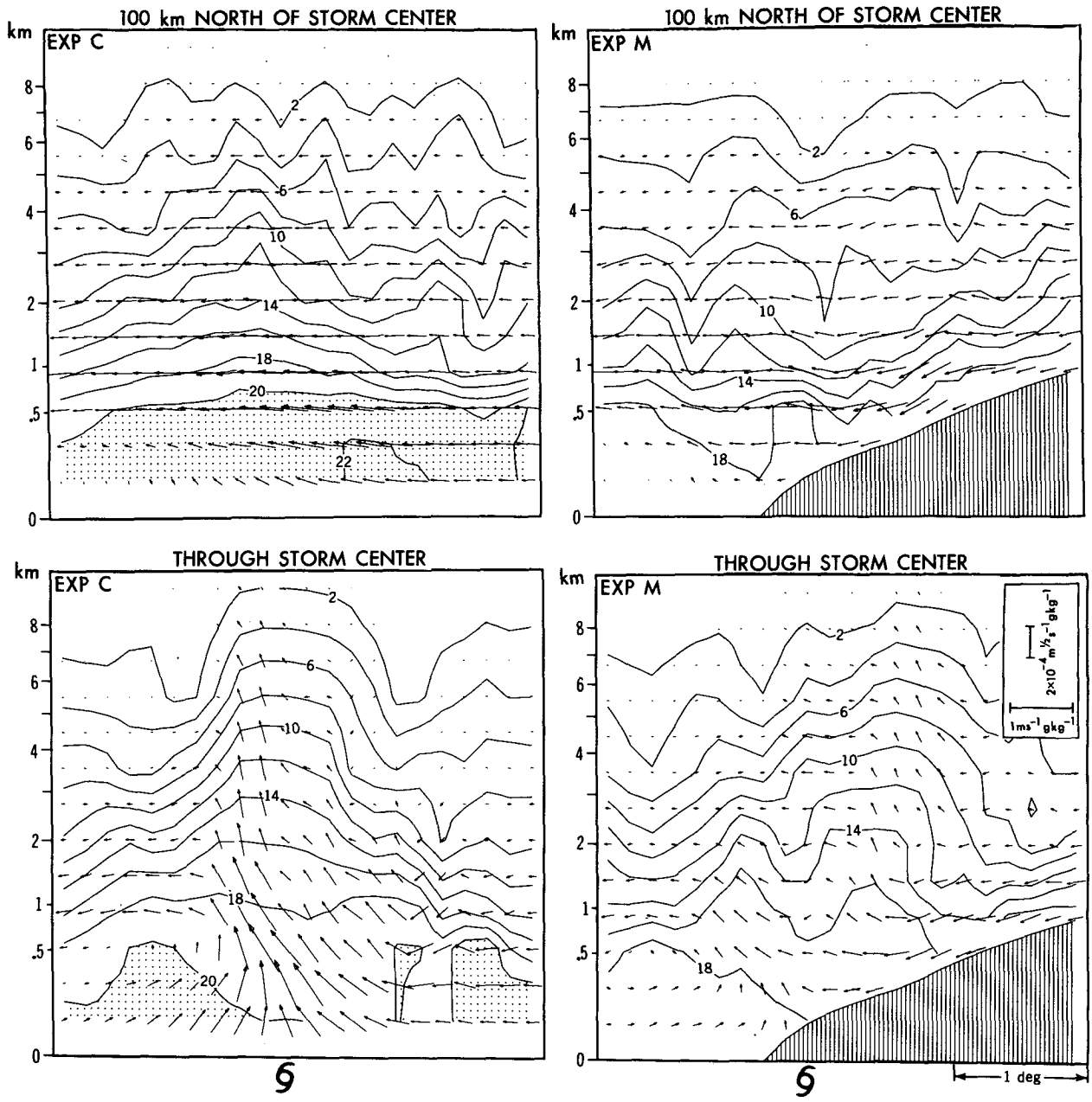

FIG. 11. East–west vertical cross section of the mixing ratio through the storm center (lower) and about 100 km to the north (upper) for both Exp. C (left side) and Exp. M (right side). All maps were obtained for the time period about 12 h after landfall. The vertical coordinate for these cross sections and for all others presented hereafter is the square root of height in meters. Accordingly, the vertical velocity component in this coordinate system is given by $d\sqrt{z}/dt$; i.e., $w = dz/dt = 2\sqrt{z}(d\sqrt{z}/dt)$. Vector arrows show the moisture flux, the components of which are $r(dx/dt)$ and $r(d\sqrt{z}/dt)$ where r is the mixing ratio. The actual height (km) is presented on the left side of each map.

mountain effect; i.e., an export of moisture out of the storm area in the boundary layer above the mountain ridge, northwest of the storm. Since the area-averaged precipitation increased sharply after landfall, this resulted in a sharp decrease in the precipitable water during the first six hours after landfall. The outflow northwest of the storm center enhanced the export of kinetic energy from the storm domain, yielding a large net decrease in the storm's total kinetic energy. As the storm approached the west base of the mountain 12 h after landfall, the reduction in the supply of available latent energy

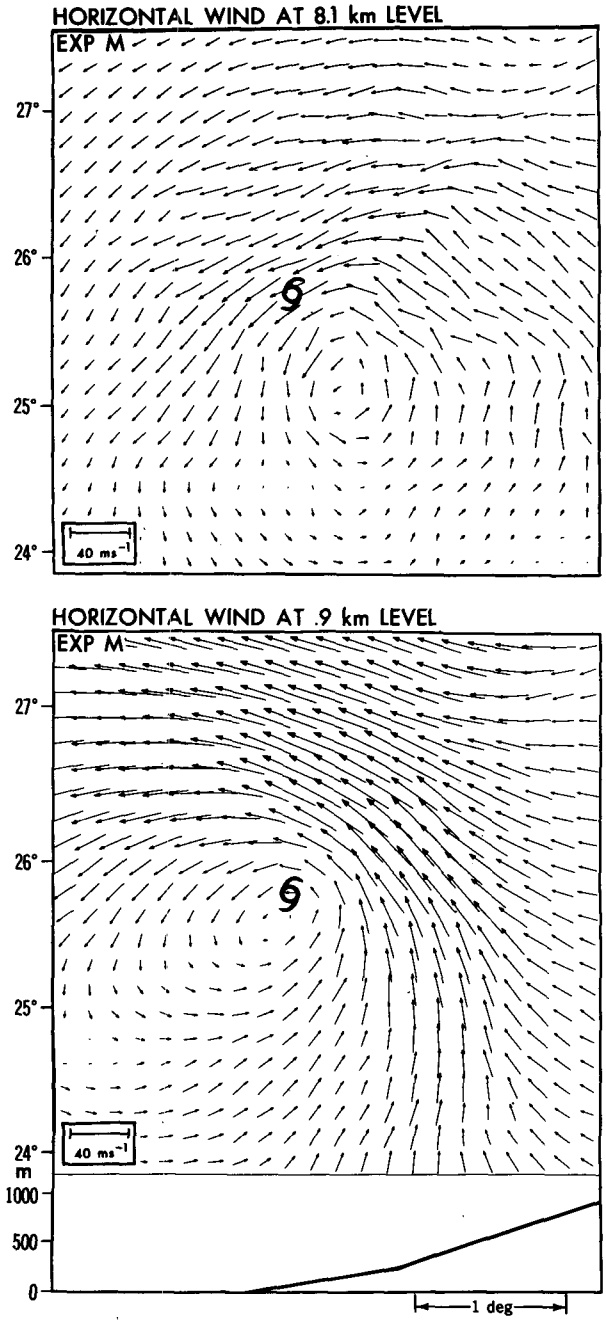

FIG. 12. Distribution of the horizontal wind vectors for Exp. M at the 8.1 km height (upper) and the 0.9 km height (lower) at 90 h. See Fig. 9 for further information.

continued because the air advected into the storm center was still considerably drier. Also, the storm was significantly more disorganized by this time, with the upper-level circulation center considerably displaced to the southeast of the lower-level circulation center. Thus, the storm continued to weaken well after landfall in Exp. M, in contrast to Exp. C.

d. Foehn effect

An interesting and important phenomenon associated with flow over mountains is the occurrence of foehn winds. A general definition of a foehn includes any warm, dry wind descending the lee of a mountain range (Brinkman, 1971). Foehn winds are not always strong, although this is usually the case. The presence of warm and dry winds descending the mountain ranges of Japan during the passage of a typhoon has been noted in the past (Okuda, 1976). In Exp. M we observed a foehnlike feature as the storm passed the top of the mountain range and the storm winds north of the center began to descend the mountain slope. Analysis of the temperature fields at 85 h, when the storm was just crossing the mountain peak, indicated anomalously warm temperatures northwest of the storm. For example, along the 200 m mountain contour, the temperature at model level 11 increased over 4°C from the center latitude of the innermost mesh to 100 km to the north. This warm region slowly shifted westward as the storm continued its descent down the mountain. By 90 h (about 12 h after landfall) the warm area was centered near the base of the mountain range, as is shown in Fig. 13.

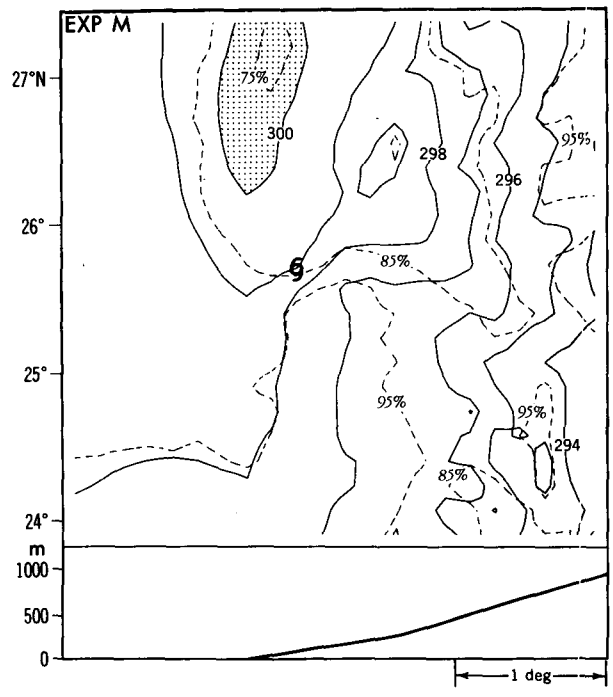

FIG. 13. Distribution of the relative humidity (dashed line) and temperature (solid line) on the lowest model level (σ = 0.992) at 90 h, or about 12 h after landfall. The area with temperatures greater than 300 K are shaded. The storm center is indicated by a tropical storm symbol. Mountain height (m) is plotted at the bottom as a function of longitude.

Air at the center of this warm region was also dry. The relative humidity along the base of the mountain varied from 92% with mixing ratios of 18.9 g kg^{-1} at the center latitude of the mesh domain to under 75% and mixing ratios of 17.6 g kg^{-1} 175 km to the north. As the storm moved away from the mountain the warm region continued to weaken, although some sign of it still remained just west of the mountain base at the end of the integration at 97 h.

The foehn effect did not seem to be significant in Exp. ZF (i.e., without the storm). In Exp. M, the descent of air down the mountain range was considerably stronger compared with Exp. ZF. Also, increased latent heating occurred on the windward side of the mountain in Exp. M. In order to examine what effects the above differences had on the foehn formation, the temperature difference between Exps. M and ZF is presented in Fig. 14. We see that a significantly greater warming did occur near the mountain base north of the storm, when the storm was descending the mountain. At the base of the mountain a maximum temperature difference of about 2.9°C was observed near the surface. Experiment M was also slightly drier at the surface near the base of the mountain, with a maximum difference in the mixing ratio of about 1 gm kg^{-1}. Figure 14 also indicates that in many places the air in Exp. M appeared cooler between 0.5 and 1 km. These anomalies appeared well correlated with upward motion regions in Exp. M. Weak subsidence occurred in most of the same regions in Exp. ZF.

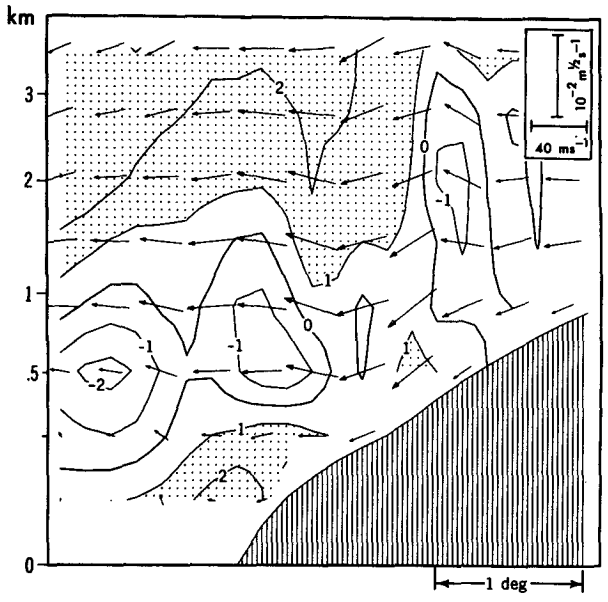

FIG. 14. East–west vertical cross section through 26.8°N (about 100 km north of the storm center for Exp. M) at 90 h for the temperature deviation of Exp. M from Exp. ZF. Analysis is shown for the lowest 3600 meters of the atmosphere. The shaded region represents points with a temperature difference of one degree or greater. The arrows plotted at every other grid point are wind vectors for Exp. M. The vertical coordinate is defined in Fig. 11.

4. Results of Exp. ZF

In order to understand the effect of the mountain on the landfalling tropical cyclone, it is important to understand changes that occurred in the basic zonal flow itself with the introduction of topography into the model. Experiment ZF, described in Section 2, was performed for this purpose. We have already shown in Fig. 3 that in both the lower and middle atmosphere the mountain range caused a significant change in the basic flow, which influenced the storm movement. In this section results of Exp. ZF are examined in more detail.

Figure 15 shows a vertical distribution of the composite flow field for two time periods for which the finest mesh was over each side of the mountain. Since the flow was almost steady at this time, particularly on the upwind side, the wind fields for the two time levels, separated by about nine hours, were combined into one figure to obtain a complete view of the flow field over the mountain region. Wind fields presented here were meridionally averaged over the entire extent of the finest mesh. The mountain induced a low-level southerly component which was strong on the lee side of the mountain and also extended well downstream from the mountain range. A distinct maximum in this southerly component of about 16 m s^{-1} occurred about 65 km from the western edge of the mountain. The existence of a low-level jet running parallel to a very long mountain ridge agrees with other numerical results obtained by Mason and Sykes (1978) and Hayes and Williams (1977).

The wavelike distribution of the vertical velocity, as shown by the wind vectors in Fig. 15, is in basic agreement with the flow pattern obtained by Queney (1948) for stratified rotating flow over a mountain with approximately the same width, height, basic wind and static stability. Actually, in Exp. ZF the static stability parameter $(g\partial \ln\theta/\partial z)^{1/2}$, calculated from the tropopause level (14.4 km) to about 1.4 km, varied from 0.98×10^{-2} s^{-1} over the mountain ridge to 0.96×10^{-2} s^{-1} over the ocean and 0.94×10^{-2} s^{-1} just west of the mountain. The vertical motion at the lower levels, induced by the orography, produced a banded pattern in the accumulated rainfall distribution (figure not shown) over the mountain range. The maximum accumulation was about 1.5 cm in 12 hours, distributed along the 500 meter height contour of the mountain on the lee side. Bands of weaker rainfall (about 0.5 cm total) occurred immediately above the mountain top, along the 400-

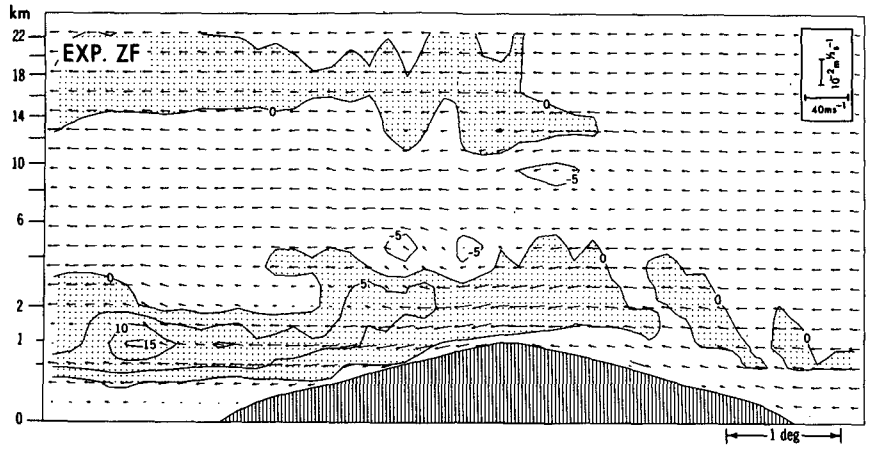

FIG. 15. East–west vertical distribution of the flow field over the entire mountain region for Exp. ZF. Wind fields presented are those averaged over the entire latitudinal extent of the innermost mesh. The figure was prepared by compositing the results at 82 and 91 h. The meridional component of the flow is contoured (m s^{-1}), with the regions of southerly flow shaded. The arrows indicate the zonal and vertical components. The vertical coordinate is defined in Fig. 11.

meter contour on the upwind side, and about 65 km west of the mountain base. Figure 16 clearly shows that the mountain waves spread well downstream and upward from the mountain slope. Analysis of several other time levels indicate that Figs. 15 and 16 represent a quasi-stationary pattern of inertia–gravity waves forced in Exp. ZF. Although the general positions of rising and sinking motion did not change with time, the individual maxima and minima did vary considerably. It is interesting to note that a negative temperature anomaly can be seen above the mountain surface in Fig. 16. This relatively low temperature just above the surface resulted from the strong heat flux into the ground as the descending air was advected over the cooler mountain slope.

Finally, one of the most interesting features that was observed in Exp. ZF was the existence of a low-level southerly wind maximum found west of the base of the mountain range. From Figs. 15 and 16 we see that this jet appeared to be associated with an inertia–gravity wave. An analysis of the momentum equation indicated that the sharp northward curving of the flow field east of this jet axis caused the inertia term to become very large negative there, which was mainly balanced by the Coriolis force produced by the southerly wind component. Within a very narrow region near the center of the jet the wind direction was nearly southerly and the inertia force became small so that the flow approached geostrophic balance.

The mountain-induced flow patterns shown in this section were altered when the tropical cyclone was present. However, it is difficult to analyze the degree of influence the mountain waves had on the storm structure and decay.

5. Summary and remarks

The landfall of a tropical cyclone was numerically simulated with the effect of a mountain range included. The mountain range influenced the decay rate and the precipitation distribution of the tropical cyclone, which is basically consistent with observations. Also, a noticeable change in the storm track was observed. The mountain, which paralleled the shoreline, was approximately 1 km high, 500 km wide and 2100 km long. When comparison of the above simulation was made with a control landfall simulation performed over flat terrain, it was found that the fill rate of the sea level pressure during the first 12 h after landfall increased from 20 to 32 mb.

To investigate the possible mechanisms that enhanced the decay rate of the storm, moisture and kinetic energy budgets were calculated for the 3.5 × 3.5° region containing the storm. It was found that relative to the control experiment the area-averaged precipitation increased sharply just before and for about seven hours after landfall. At the same time, the net flux convergence of moisture into the storm area decreased, resulting in a sharp decrease in the precipitable water. Analysis of the kinetic energy budget indicated that the net divergence of kinetic energy away from the storm region increased relative to the control case, yielding a net decrease in the storm's total kinetic energy after landfall. As the tropical cyclone descended down the lee side of the mountain range the low-level moisture fields were significantly drier, causing a reduced supply of moisture into the storm region. Also, the storm was significantly more disorganized, with the upper-level

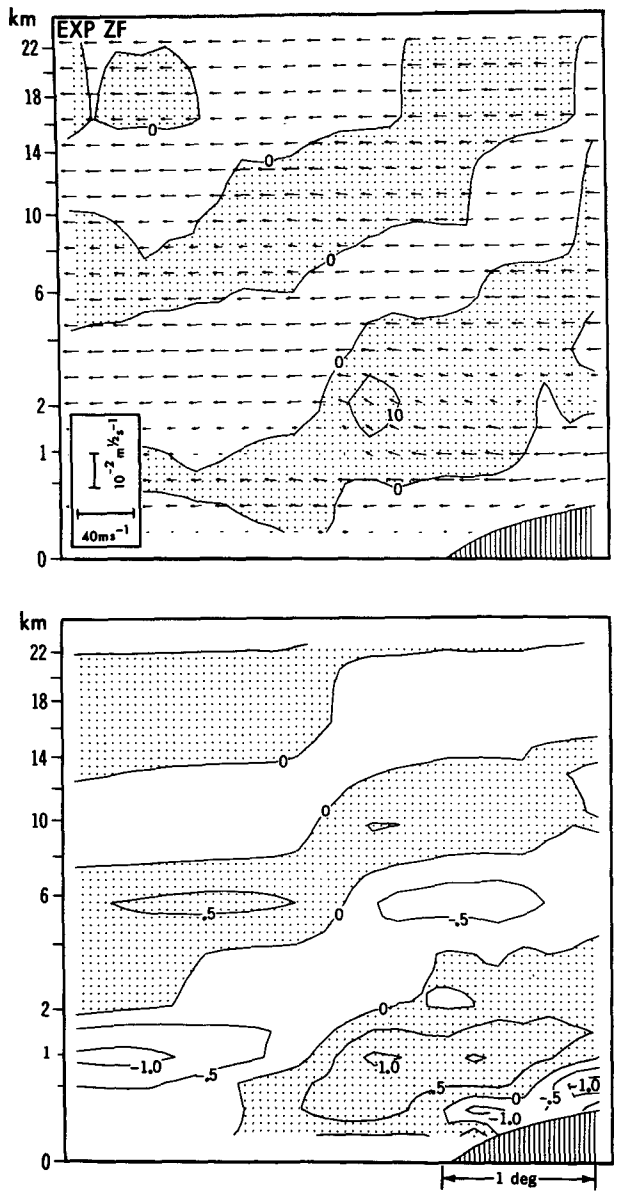

FIG. 16. East–west vertical distribution of the zonal-vertical wind vectors for Exp. ZF at 94 h (upper figure) averaged over the entire latitudinal extent of the innermost mesh area. Upward motion ($w > 0$) is shaded with w contoured (cm s^{-1}). The deviation of the temperature (K) from the horizontally averaged temperature for the domain is also presented (bottom figure). Areas with positive deviation are shaded. The vertical coordinate is defined in Fig. 11.

circulation center displaced well to the southeast of the lower-level circulation center. Thus, the storm continued to decay beyond 12 h after landfall.

Rainfall analyses showed that the heaviest precipitation after landfall was located primarily to the north of the storm track for most of the distance up the mountain, where forced ascent of the wind occurred. It was also shown that after 82 h (4 h after landfall), the area of heavier precipitation began to slowly shift clockwise relative to the storm with most of the significant precipitation falling to the southeast of the storm center by 87 h.

Finally, from a supplemental experiment, we found that the mountain range caused a significant change in the basic flow over the mountain. When the tropical cyclone was present this caused the storm to veer to the south relative to the control as it ascended the mountain range. As the storm descended the other side, the basic flow produced a northward storm movement which was slightly more than double the northward displacement in the control case.

Although the present experiment was performed for an idealized distribution of topography, some of the important effects that mountain ranges may have on landfalling tropical cyclones were reproduced. The simplifications in the basic experimental design enabled these effects to be easily isolated and analyzed in detail. It is believed that this has led to an improved understanding of the mountain effects. It is uncertain how these effects will vary with more realistic topographic distributions, although we expect that they will exhibit considerable variation with the particular mountain scale and basic flow being considered. An additional factor to be considered that influences a storm after landfall is the storm's encounter with continental air masses or other weather systems. These problems will be addressed in future studies.

Acknowledgments. The authors would like to thank I. Orlanski and J. Mahlman for their continuous support of the hurricane dynamics project at GFDL. They are grateful to R. Pierrehumbert of GFDL for his suggestions and comments during the course of this study. They would also like to express their appreciation to S. Lyons of GFDL, S. Chang of the Naval Research Laboratory and B. Carissimo of the GFD Program, Princeton University, for their valuable comments and criticisms on the original version of this manuscript. Special credit is also given to P. Tunison, M. Zadworny, J. Varanyak, K. Raphael and J. Conner for preparing the figures, and to J. Kennedy for typing the manuscript.

REFERENCES

Anthes, R. A., 1982: *Tropical Cyclones—Their Evolution, Structure, and Effects. Meteor. Monogr.* No. 41, Amer. Meteor. Soc., 208 pp. [ISBN 0-933876-54-8.]

——, and S. W. Chang, 1978: Response of the hurricane boundary layer to changes of sea surface temperature in a numerical model. *J. Atmos. Sci.*, **35**, 1240–1255.

Brand, S., and J. W. Blelloch, 1973: Changes in the characteristics of typhoons crossing the Philippines. *J. Appl. Meteor.*, **12**, 104–109.

——, and ——, 1974: Changes in the characteristics of typhoons crossing the island of Taiwan. *Mon. Wea. Rev.*, **102**, 708–713.

Brinkman, W. A., 1971: What is a foehn? *Weather*, **26**, 230–239.

Brunt, A. T., 1968: Space-time relations of cyclone rainfall in the northeast Australian region. *Civil Eng. Trans. Inst. Eng. Australia,* April issue, 40–46. Inst. of Eng., Australia, 11 National Circuit, Barton, A.C.T. 2600, Australia.

Chang, S. W., 1982: The orographic effects induced by an island mountain range on propagating tropical cyclones. *Mon. Wea. Rev.,* **110,** 1255–1270.

Hamuro, M., Y. Kawata, S. Matsuda, T. Matsuno, N. Nakamura, F. Pak, T. Takeda and M. Yanai, 1969: Precipitation bands of Typhoon Vera in 1959 (Part 1). *J. Meteor. Soc. Japan,* **47,** 298–308.

Hays, J. L., and R. T. Williams, 1977: Numerical simulations of air flow over mountains. Tech. Rep. NPS-63 Wu7741, Naval Postgraduate School, Monterey, CA 93940.

Hebert, P. J., 1980: Atlantic hurricane season of 1979. *Mon. Wea. Rev.,* **108,** 973–990.

Hope, J. R., 1975: Atlantic hurricane season of 1974. *Weatherwise,* **28,** 12–18.

Kurihara, Y., 1973: A scheme of moist convective adjustment. *Mon. Wea. Rev.,* **101,** 547–553.

——, and M. A. Bender, 1980: Use of a movable nested-mesh model for tracking a small vortex. *Mon. Wea. Rev.,* **108,** 1792–1809.

Manabe, S., and J. L. Holloway, 1975: The seasonal variation of the hydrologic cycle as simulated by a global model of the atmosphere. *J. Geophys. Res.,* **80,** 1617–1649.

Mason, P. J., and R. I. Sykes, 1978: On the interaction of topography and Ekman boundary layer pumping in a stratified atmosphere. *Quart. J. Roy. Meteor. Soc.,* **104,** 475–490.

Mellor, G. L., and T. Yamada, 1974: A hierarchy of turbulence closure models for planetary boundary layers. *J. Atmos. Sci.,* **31,** 571–583.

Miller, B., 1964: A study of the filling of hurricane Donna (1960) over land. *Mon. Wea. Rev.,* **92,** 389–406.

Moss, M. S., and R. W. Jones, 1978: A numerical simulation of hurricane landfall. NOAA Tech. Memo. ERL NHEML-3, NOAA/AOML/HRD, Boulder, CO, 1–15.

Okuda, Y., 1976: Typhoon disasters. Kisyo-Kenkyu Note No. 129, Meteor. Soc. of Japan, Chiyoda-ku, Tokyo, Japan. 267 pp. (In Japanese.)

Pierrehumbert, R. T., 1984: Linear results on the barrier effects of mesoscale mountains. *J. Atmos. Sci.,* **41,** 1356–1367.

Queney, P., 1948: The problem of airflow over mountains. A summary of theoretical studies. *Bull. Amer. Meteor. Soc.,* **29,** 16–26.

Simpson, R. H., and H. Riehl, 1981: *The Hurricane and Its Impact.* Louisiana State University Press, 398 pp. [ISBN 0-8071-0688-7.]

Smith, R. B., 1979: The influence of mountains on the atmosphere. *Advances in Geophysics,* Vol. 21, Academic Press, 87–230.

Suda, T., 1972: Orographic effects of the Himalayas on the formation and movement of typhoons and extratropical cyclones. *J. Meteor. Res.,* **24,** 495–509. (In Japanese.)

Tuleya, R. E., and Y. Kurihara, 1978: A numerical simulation of the landfall of tropical cyclones. *J. Atmos. Sci.,* **35,** 242–257.

——, M. A. Bender and Y. Kurihara, 1984: A simulation study of the landfall of tropical cyclones using a movable nested-mesh model. *Mon. Wea. Rev.,* **112,** 124–136.